

# Deformable Attention Graph Representation Learning for Histopathology Whole Slide Image Analysis

Mingxi Fu<sup>1\*</sup>, Xitong Ling<sup>1\*</sup>, Yuxuan Chen<sup>1</sup>, Jiawen Li<sup>1</sup>, Fanglei Fu<sup>1</sup>, Huaitian Yuan<sup>1</sup>, Tian Guan<sup>1†</sup>, Yonghong He<sup>1†</sup>, Lianghui Zhu<sup>1†</sup>

<sup>1</sup>Shenzhen International Graduate School, Tsinghua University

## Abstract

Accurate classification of Whole Slide Images (WSIs) and Regions of Interest (ROIs) is a fundamental challenge in computational pathology. While mainstream approaches often adopt Multiple Instance Learning (MIL), they struggle to capture the spatial dependencies among tissue structures. Graph Neural Networks (GNNs) have emerged as a solution to model inter-instance relationships, yet most rely on static graph topologies and overlook the physical spatial positions of tissue patches. Moreover, conventional attention mechanisms lack specificity, limiting their ability to focus on structurally relevant regions. In this work, we propose a novel GNN framework with deformable attention for pathology image analysis. We construct a dynamic weighted directed graph based on patch features, where each node aggregates contextual information from its neighbors via attention-weighted edges. Specifically, we incorporate learnable spatial offsets informed by the real coordinates of each patch, enabling the model to adaptively attend to morphologically relevant regions across the slide. This design significantly enhances the contextual field while preserving spatial specificity. Our framework achieves state-of-the-art performance on four benchmark datasets (TCGA-COAD, BRACS, gastric intestinal metaplasia grading, and intestinal ROI classification), demonstrating the power of deformable attention in capturing complex spatial structures in WSIs and ROIs.

## Introduction

In computational pathology, the ultra-high resolution of Whole Slide Images (WSIs) makes pixel-level annotation prohibitively time-consuming (Kumar, Gupta, and Gupta 2020), motivating the development of weakly supervised learning techniques (Afonso et al. 2024). Most existing approaches adopt embedding-based Multiple Instance Learning (MIL) frameworks (Li, Li, and Eliceiri 2021; Yao et al. 2020; Maron and Lozano-Pérez 1997), which divide a WSI into instance patches and aggregate their features for classification. However, such methods typically neglect the structural correlations between patches, making it difficult to capture the global tissue architecture and spatial dependencies, which are critical for accurate diagnosis (Wang et al. 2024a).

\*These authors contributed equally.

†Corresponding author.

Copyright © 2026, Association for the Advancement of Artificial Intelligence (www.aaai.org). All rights reserved.

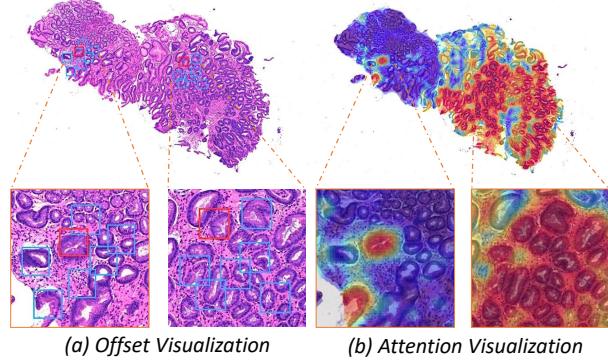


Figure 1: Deformable attention graph representation learning with learnable offsets on pathological images.

Graph Neural Networks (GNNs) have recently emerged as a powerful alternative to address this limitation (Ahmedt-Aristizabal et al. 2022). By modeling the topological relationships between tissue patches, GNNs can capture structural and spatial interactions among key regions (Chan et al. 2023). Nevertheless, most GNN-based methods rely on static graph structures and disregard the actual spatial coordinates of instances in the WSIs (Li et al. 2024). This is problematic because spatial context often determines pathological relevance; for example, ductal carcinoma in situ (DCIS) appears within the myoepithelium (Russell et al. 2015), and the loss of surface differentiation in gastric mucosa often indicates malignancy (Khazaaleh et al. 2024).

Transformer-based architectures, empowered by their strong self-attention mechanisms, are capable of modeling interactions among different instances (Shao et al. 2021). However, standard global self-attention suffers from a quadratic computational complexity with respect to the input size, which leads to prohibitive memory and computational costs when processing high-resolution images such as WSIs (Vaswani et al. 2017). To address this limitation, researchers have proposed various efficient attention mechanisms. For instance, Sparse Attention reduces the complexity through sparse connections (Child et al. 2019), Local Window Attention restricts attention computation to local regions to reduce the receptive field (Liu et al. 2021), and

Pyramid Vision Transformer utilizes a hierarchical pyramid structure to achieve multi-scale representations with reduced overhead (Wang et al. 2021). Despite their effectiveness, most of these methods rely on fixed or regularized attention patterns, which struggle to adaptively focus on structurally complex or semantically sparse regions in the image. To address this, deformable attention mechanisms (Xia et al. 2022) introduce learnable sampling offsets that dynamically attend to key spatial positions, achieving a balance between modeling flexibility and computational efficiency. While extensively used in natural image tasks, directly applying deformable attention to gigapixel-scale pathology images remains infeasible due to resolution constraints (Zhu et al. 2020).

In this work, we propose a novel Deformable Attention Graph (DAG) to tackle bag-level classification tasks in Figure 1. We first treat each patch as a graph node and construct a weighted directed graph by learning edge weights based on feature similarity between head and tail nodes. Based on this, we incorporate a deformable attention module guided by the actual spatial coordinates of each patch. This enables the model to dynamically attend to morphologically relevant regions and better adapt to complex tissue structures. We conduct extensive experiments on two public benchmarks (TCGA-COAD for cancer grading and BRACS for breast cancer subtyping) and two in-house clinical datasets (gastric intestinal metaplasia grading and intestinal ROI classification). Compared to state-of-the-art WSI analysis methods and through comprehensive ablation studies, DAG demonstrates superior performance and strong generalization capability in both WSIs and ROIs classification tasks.

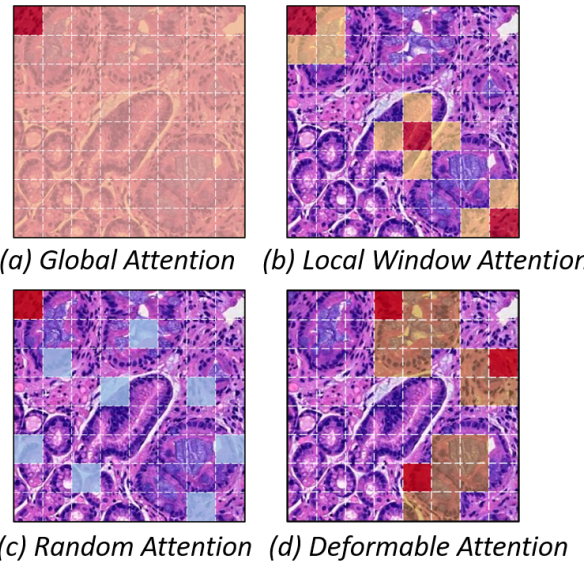


Figure 2: Comparison of different attention mechanisms: (a) Global attention spans the entire feature space. (b) Local window attention focuses on the current position and its neighboring regions. (c) Random attention establishes connections between randomly selected positions. (d) Deformable attention focuses on morphological contours dynamically.

## Related Work

### Attention Mechanisms in WSIs Analysis

MIL techniques with different attention mechanisms in Figure 2 have achieved remarkable success in weakly supervised WSI analysis by adaptively learning instance weights and prioritizing diagnostically informative regions (Gadermayr and Tschuchnig 2024). ABMIL uses the global attention to each patch for key instance aggregation, but it ignores the spatial positions and structural relationships among patches, limiting its ability to capture local-global tissue dependencies (Ilse, Tomczak, and Welling 2018). Li et al. (Li et al. 2022) introduced window-based attention, reducing the computational complexity of global attention and enhancing efficiency. Furthermore, the BigBird model (Zaheer et al. 2020) combines sliding window attention with sparse global and random attention patterns, enabling efficient modeling of long-range dependencies.

To overcome these limitations, deformable attention mechanisms have been proposed (Zhu et al. 2019). By introducing learnable offsets, these mechanisms enable the model to dynamically attend to key locations and better model structural contours (Li et al. 2021). Recently, such mechanisms have demonstrated strong performance in vision transformer architectures. For example, Xia et al. proposed the Deformable Attention Transformer (DAT), which achieved outstanding results on image classification and dense prediction tasks (Xia et al. 2022). Moreover, an enhanced version named DAT++ is built upon the DAT, achieving state-of-the-art performance on various classification and segmentation tasks in natural image domains (Xia et al. 2023). However, existing deformable attention methods are primarily designed for natural images and typically operate by locating offset sampling points directly on the input image. In the case of ultra-high-resolution whole slide images (WSIs), it is infeasible to put the entire WSIs into the network for offset computation due to memory and computational constraints.

### Graph Representation in WSIs Analysis

In recent years, GNNs have demonstrated great potential in histopathological image classification tasks (Jaume et al. 2021). Unlike traditional MIL methods, GNNs construct graph structures to effectively model the spatial and structural relationships between cells or tissue regions. Early approaches typically relied on static graph structures. For example, ABMIL-GCN embeds patch-level features into a graph and leverages attention mechanisms to capture context-aware information (Liang et al. 2023). However, it often neglects explicit structural dependencies between patch nodes. To better model spatial hierarchies, recent methods have introduced hierarchical representation strategies. Wang et al. proposed a Connectivity-Aware Graph Transformer (CGT), which enhances graph representation by integrating connection information into the node features of each graph transformer layer, significantly improving breast cancer subtype classification performance (Wang et al. 2024b). HACT-Net introduced a hierarchical GNN that models cell-to-tissue level structures, leading to improved

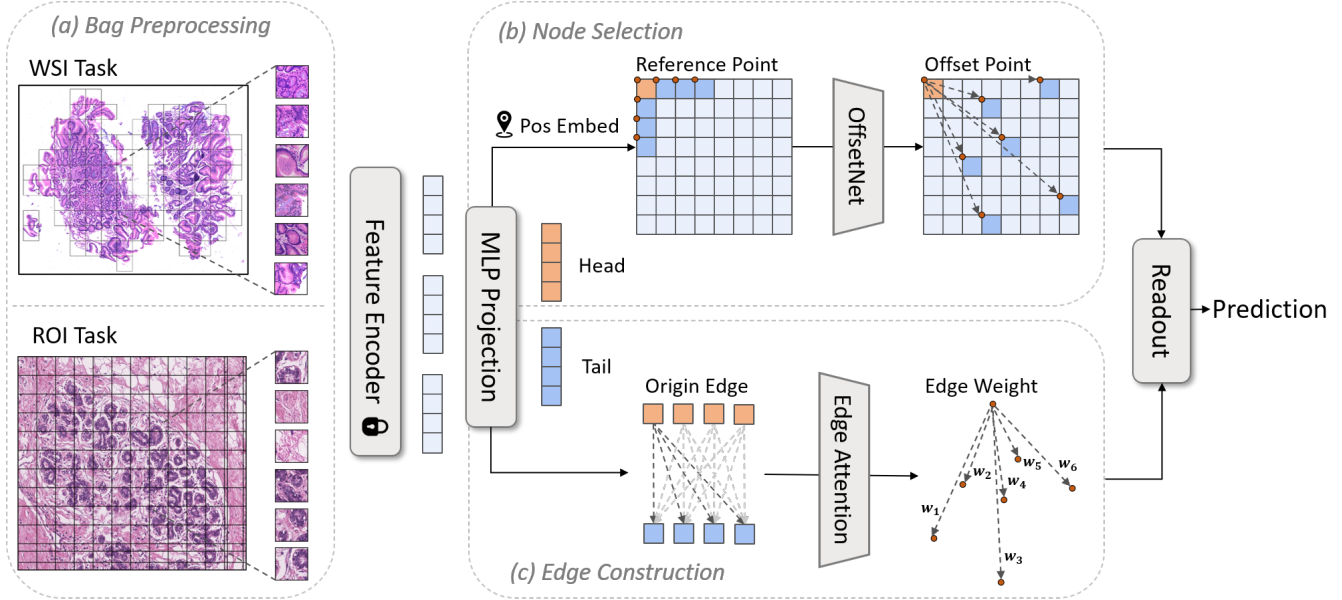


Figure 3: Overall process: (a) The preprocessing of WSIs and ROIs. (b) Node selection through offsetnet in graph network. (c) Dynamic weighted edge construction in graph network.

multi-class classification of breast cancer subtypes (Pati et al. 2020). In terms of modeling long-range dependencies, Su et al. combined GNNs and transformers in HAT-Net to better capture both structural and contextual information, achieving strong performance on colorectal cancer grading tasks (Su et al. 2021).

To overcome the limitations of static graph structures in modeling distant structural dependencies, WiKG reformulates WSIs as knowledge graphs and constructs dynamic graph representations to enable end-to-end learning (Li et al. 2024). Similarly, Chen et al. proposed a dynamic hypergraph neural network (DyHG) using connect multiple nodes to overcome the constraints of fixed graph topologies (Chen et al. 2025). Despite these advances, most existing methods overlook the actual physical locations of patches during graph construction and lack mechanisms to model edge weights. These limitations hinder the expressive power of GNNs when dealing with the complex spatial structures inherent in WSIs.

## Methodology

### Deformable Graph Construction

Given a WSI, we first segment the foreground regions using the OTSU thresholding method in Figure 3. Then, we apply a sliding window operation to divide the WSIs into non-overlapping patches  $P = \{p_1, p_2, \dots, p_N\}$ , where each patch is regarded as a graph node. We extract features from each patch using pretrained pathology models (e.g., UNI (Chen et al. 2024)). Each patch also has its real-world coordinate  $coord = \{(x_1, y_1), (x_2, y_2), \dots, (x_N, y_N)\}$ , where  $c_i = (x_i, y_i)$  denotes the location of the  $i$ -th patch. Based on this, we construct a directed graph where each node has both a head and a tail representation. The head

node focuses on discovering the relationships between itself and other patches, while the tail node evaluates its own contribution to the head nodes.

$$h_i = W_h f(P), \quad t_i = W_t f(P), \quad (1)$$

where  $h_i$  and  $t_i$  respectively denote the head and tail embeddings of patch  $i$ . Traditional deformable attention typically samples from a uniformly distributed reference grid and learns offsets for each point, which are used to sample neighboring positions. Inspired by this idea, we transform the entire WSI into a set of reference points, then input each head node into a lightweight network  $\mathcal{O}_{\text{offset}}(\cdot)$  to generate  $K$  pixel-level offsets  $O_i = \{o_{i,1}, o_{i,2}, \dots, o_{i,K}\}$ :

$$O_i = \{i \in \mathcal{V} : o_i = \mathcal{O}_{\text{offset}}(h_i)\}, \quad (2)$$

where  $\mathcal{V}$  is the set of patch nodes and  $|\mathcal{V}| = N$ ,  $|O_i| = K$ . To dynamically normalize these offsets for better neighbor sampling, we apply the following transformation:

$$O_i = O_i \times S \times \sqrt{N} \times \sigma(\alpha), \quad (3)$$

where  $S$  denotes the spatial stride used for feature extraction, which maps the offset from the feature space back to the original image space. Let  $N$  be the number of patches in each WSI. To account for different WSI sizes, we normalize the offset using the patch number  $N$  and use a learnable parameter  $\alpha$  activated through a sigmoid function to adjust the offset scale dynamically.

Previous studies often construct implicit structures purely based on relative patch locations while ignoring the absolute spatial positions of patches. To address this, we incorporate the actual spatial coordinates of each patch to generate deformable query positions as follows:

$$q_{i,k} = c_i + o_{i,k}, \quad k = 1, \dots, K, \quad (4)$$

where  $q_{i,k}$  represents the position of the  $k$ -th query point of the  $i$ -th patch after applying the offset, which defines the dynamically updated attention field. Next, we calculate the Euclidean distance between each query point  $q_{i,k}$  and all real patch coordinates  $c_j$ , and find the closest real patch  $c_j$  as its neighbor:

$$D_{i,k} = \arg \min_{j \in \{1, \dots, N\}} \|q_{i,k} - c_j\|_2^2, \quad (5)$$

where  $i$  denotes the head node,  $k$  is the query index, and  $j$  is the tail node. For each of the  $K$  queries of node  $i$ , we obtain a neighbor set as:

$$n_{i,k} = t_{D_{i,k}}. \quad (6)$$

Finally, the full set of dynamically sampled neighbors for node  $i$  under the deformable graph structure is  $N_i = \{n_{i,1}, n_{i,2}, \dots, n_{i,K}\}$ .

### Dynamic Edge Weights Learning

To fully leverage the offset information gained from the graph, we design an attention mechanism that weights neighbors using both the head and tail node features as well as the learned offsets. Specifically, we first expand the head node feature  $h_i$  via linear transformation. Then, for each pair of head node and neighbor node, we compute their cosine similarity as:

$$s_{i,k} = \frac{(h_i \cdot n_{i,k})^\top}{\|h_i\|_2 \|n_{i,k}\|_2}. \quad (7)$$

We then apply softmax normalization over the  $K$  neighbors of node  $i$ :

$$\alpha_{i,k} = \frac{\exp(s_{i,k})}{\sum_{k=1}^K \exp(s_{i,k})}, \quad (8)$$

where  $\alpha_{i,k}$  denotes the attention weight for the  $k$ -th edge of node  $i$ , indicating the influence strength of the  $k$ -th neighbor node. It guides the message passing from the tail node to the head node. Besides, we use a gating mechanism to fuse head and neighbor node features, while also learning the difference between them:

$$u_{i,k} = \tanh(h_i + \alpha_{i,k} \cdot n_{i,k}), \quad (9)$$

$$e_i = \text{Softmax}(u_{i,k} \cdot n_{i,k}), \quad (10)$$

where  $e_i$  represents the aggregated neighbors information after updated attention. We then fuse  $e_i$  with the original head feature to form an updated representation for the head node, which will be used for downstream classification. To further enhance information flow between nodes, we adopt a dual-channel residual fusion mechanism:

$$h_i = \sigma_1(W_1(h_i + e_i)) + \sigma_2(W_2(h_i \odot e_i)), \quad (11)$$

where  $\sigma$  represents an activation function such as LeakyReLU, and  $W_1, W_2$  are learnable projection matrices. Finally, a global readout function is used to aggregate patch-level representations into slide-level representation for classification:

$$\hat{Y} = \text{Softmax}(\text{Readout}(G)). \quad (12)$$

The Readout function can be instantiated as global average pooling, max pooling, or attention-based pooling, where  $\hat{Y}$  is the predicted class probability for the WSI.

## EXPERIMENT

### Datasets

We evaluate our proposed method on four datasets, covering both WSIs and ROIs level classification tasks. Specifically, we use two WSI-level datasets: the publicly available TCGA-COAD and a private gastric intestinal metaplasia grading dataset; and two ROI-level datasets: the publicly available BRACS breast cancer subtyping dataset and a private intestinal cancer classification dataset.

**TCGA-COAD (Public WSI dataset).** This dataset includes 465 WSIs from the TCGA Colon Adenocarcinoma (TCGA-COAD) cohort. The cases are categorized into four classes: Adenomas and Adenocarcinomas (388), Cystic, Mucinous and Serous Neoplasms (60), Complex Epithelial Neoplasms (11), and Epithelial Neoplasms, NOS (6).

**Gastric intestinal metaplasia (Private WSI dataset).** This dataset is collected from the Second Affiliated Hospital of Southern University of Science and Technology. It contains 984 gastric WSIs diagnosed with different grades of intestinal metaplasia, including 309 slides without metaplasia, 299 with mild metaplasia, 107 with moderate metaplasia, and 269 with severe metaplasia.

**BRACS (Public ROI dataset).** This dataset contains 4492 ROIs related to breast cancer subtypes. It covers seven categories: benign (833), usual ductal hyperplasia (UDH, 506), flat epithelial atypia (FEA, 754), atypical ductal hyperplasia (ADH, 503), ductal carcinoma in situ (DCIS, 783), invasive carcinoma (647), and normal tissue (466).

**Intestinal cancer classification (Private ROI dataset).** This dataset consists of ROIs extracted from WSIs of intestinal tissues provided by the Chongqing University Affiliated Three Gorges Hospital. It includes a total of 9381 ROIs, categorized into four classes: cancer (3591), high-grade intraepithelial neoplasia (767), low-grade intraepithelial neoplasia (2982), and non-tumor (2041).

We report the mean and standard deviation of three standard evaluation metrics: accuracy (ACC), weighted F1-score, and area under the ROC curve (AUCROC).

### Implementation Details

During the pre-processing stage, WSI-level datasets are partitioned into non-overlapping patches of size  $1024 \times 1024$  at  $10\times$  magnification, while ROI-level datasets are divided into non-overlapping patches of  $256 \times 256$  pixels. All experiments are conducted using consistent hyperparameters on a workstation equipped with NVIDIA RTX A100 GPUs. We employ the UNI model as the feature encoder, which is pre-trained on histopathological images (Chen et al. 2024). All tasks are evaluated using 5-fold cross-validation, with the training, validation, and test sets split in a ratio of 7:2:1. During training, we use the cross-entropy loss, the Adam optimizer with a base learning rate of 0.001, and a weight decay coefficient of 1e-5. Training is conducted for 70 epochs, and model performance is monitored using validation accuracy. Early stopping is applied with a patience of 30 epochs.

Method	TCGA-COAD			Gastritis-IM			BRACS			Intestine		
	ACC	AUC	F1									
ABMIL	86.24 <sub>1.40</sub>	95.38 <sub>0.24</sub>	84.39 <sub>1.11</sub>	78.36 <sub>3.07</sub>	94.12 <sub>0.86</sub>	75.71 <sub>3.27</sub>	57.60 <sub>1.19</sub>	90.05 <sub>0.30</sub>	56.56 <sub>1.47</sub>	94.67 <sub>0.40</sub>	99.36 <sub>0.12</sub>	94.62 <sub>0.41</sub>
AMDMIL	85.81 <sub>2.07</sub>	95.38 <sub>0.15</sub>	84.21 <sub>1.59</sub>	79.11 <sub>3.28</sub>	94.55 <sub>1.73</sub>	79.10 <sub>2.53</sub>	58.47 <sub>2.36</sub>	89.14 <sub>2.39</sub>	57.03 <sub>2.28</sub>	96.16 <sub>0.48</sub>	99.36 <sub>0.20</sub>	96.15 <sub>0.48</sub>
CLAM-SB	86.67 <sub>0.96</sub>	93.65 <sub>0.34</sub>	84.00 <sub>1.06</sub>	79.47 <sub>1.42</sub>	94.98 <sub>0.54</sub>	78.58 <sub>1.20</sub>	56.22 <sub>2.62</sub>	89.24 <sub>0.68</sub>	55.86 <sub>2.02</sub>	96.14 <sub>1.24</sub>	99.20 <sub>0.56</sub>	96.14 <sub>0.53</sub>
FRMIL	84.09 <sub>2.07</sub>	92.38 <sub>1.11</sub>	80.26 <sub>2.23</sub>	73.98 <sub>1.77</sub>	90.50 <sub>1.75</sub>	72.96 <sub>2.13</sub>	55.96 <sub>1.90</sub>	84.01 <sub>3.39</sub>	55.72 <sub>1.77</sub>	83.58 <sub>1.64</sub>	94.15 <sub>0.86</sub>	83.44 <sub>1.63</sub>
TransMIL	86.45 <sub>1.95</sub>	95.07 <sub>0.98</sub>	83.70 <sub>2.46</sub>	77.84 <sub>3.11</sub>	94.50 <sub>0.69</sub>	76.77 <sub>2.08</sub>	55.38 <sub>1.50</sub>	89.35 <sub>0.70</sub>	55.21 <sub>1.34</sub>	88.28 <sub>1.77</sub>	98.12 <sub>0.32</sub>	87.90 <sub>1.97</sub>
DM-GNN	86.67 <sub>1.23</sub>	94.40 <sub>0.66</sub>	84.36 <sub>1.20</sub>	78.15 <sub>1.05</sub>	93.99 <sub>0.88</sub>	77.48 <sub>1.82</sub>	57.27 <sub>1.34</sub>	89.26 <sub>1.65</sub>	55.68 <sub>1.34</sub>	96.22 <sub>0.48</sub>	99.30 <sub>0.11</sub>	96.26 <sub>0.49</sub>
DyHG	86.67 <sub>1.63</sub>	95.18 <sub>0.67</sub>	84.42 <sub>2.39</sub>	79.59 <sub>2.67</sub>	93.42 <sub>2.81</sub>	78.95 <sub>1.44</sub>	58.91 <sub>1.47</sub>	90.13 <sub>0.22</sub>	57.79 <sub>1.50</sub>	96.21 <sub>0.63</sub>	99.35 <sub>0.32</sub>	96.19 <sub>0.63</sub>
Patch-GCN	85.81 <sub>0.90</sub>	94.52 <sub>1.30</sub>	81.54 <sub>3.23</sub>	73.98 <sub>2.27</sub>	91.60 <sub>1.56</sub>	71.12 <sub>2.65</sub>	54.47 <sub>1.96</sub>	86.07 <sub>0.91</sub>	54.19 <sub>1.52</sub>	89.92 <sub>1.39</sub>	97.95 <sub>0.20</sub>	89.79 <sub>1.43</sub>
WiKG	85.81 <sub>3.26</sub>	94.19 <sub>1.20</sub>	83.72 <sub>2.83</sub>	76.62 <sub>5.65</sub>	93.67 <sub>2.02</sub>	74.95 <sub>4.97</sub>	57.78 <sub>2.85</sub>	89.95 <sub>0.67</sub>	56.89 <sub>2.93</sub>	94.69 <sub>0.90</sub>	99.21 <sub>0.20</sub>	94.64 <sub>0.91</sub>
DAG	<b>87.31<sub>1.59</sub></b>	<b>95.73<sub>0.56</sub></b>	<b>84.89<sub>1.50</sub></b>	<b>80.39<sub>2.60</sub></b>	<b>95.24<sub>0.48</sub></b>	<b>79.27<sub>3.48</sub></b>	<b>59.67<sub>1.34</sub></b>	<b>90.20<sub>0.81</sub></b>	<b>58.11<sub>1.17</sub></b>	<b>96.36<sub>1.42</sub></b>	<b>99.46<sub>0.20</sub></b>	<b>96.33<sub>1.46</sub></b>

Table 1: Performance of DAG on TCGA-COAD, Gastric intestinal metaplasia, BRACS, and Intestinal cancer datasets.

### Comparison with State-of-the-Art Methods

In this study, we present the experimental results of our proposed DAG framework on four datasets and compare it against both traditional MIL methods and graph-based approaches. Specifically, we compare with (1) ABMIL (Ilse, Tomczak, and Welling 2018), a classical MIL method that aggregates instance features via attention to generate bag-level embeddings; (2) AMDMIL (Ling et al. 2024), which introduces an agent aggregator with a mask denoising mechanism for WSI analysis; (3) CLAM-SB (Lu et al. 2021), a gated attention-based MIL framework optimized using a clustering-constrained loss to improve instance selection; (4) FRMIL (Chikontwe et al. 2024), which recalibrates WSI bag distributions by leveraging statistics from critical instances; (5) TransMIL (Shao et al. 2021), a transformer-based MIL method incorporating multiscale position encodings to capture inter-instance dependencies; (6) DM-GNN (Wang et al. 2024c), a dual-stream graph network equipped with affinity-guided attention recalibration for robust global graph representation; (7) DyHG (Chen et al. 2025), a dynamic hypergraph network that constructs hyperedges via Gumbel-Softmax-based nonlinear transformations; (8) Patch-GCN (Chen et al. 2021), a hierarchical graph model designed for WSIs analysis using global attention pooling; and (9) WIKG (Li et al. 2024), which conceptualizes WSIs as dynamic knowledge graphs for end-to-end graph learning. Our DAG framework consistently outperforms these baselines across WSIs and ROIs level classification tasks, demonstrating its effectiveness in modeling weighted spatial relationships in histopathological images.

As shown in Table 1, our proposed DAG model achieves the best performance across all four tasks, including two WSI-level tasks (TCGA-COAD and Gastritis-IM) and two ROI-level tasks (Intestine and BRACS). Compared to the second-best methods, DAG has improvements in accuracy, with gains of 0.64% on TCGA-COAD, 0.8% on Gastritis-IM, 0.76% on BRACS, and 0.14% on Intestine. These results demonstrate that DAG can effectively adapt to the

complex spatial distribution of WSIs while capturing fine-grained structural variations.

### Interpretability Analysis

To further evaluate the advantages of our proposed DAG method in lesion localization, we conducted a visual comparison on representative WSIs of Gastric intestinal metaplasia dataset with several mainstream MIL and graph-based models, including ABMIL (Ilse, Tomczak, and Welling 2018), TransMIL (Shao et al. 2021), WIKG (Li et al. 2024), and DAG, as shown in Figure 4. The red annotations in the ‘Official annotation’ column indicate the ground-truth lesion regions provided by pathologists.

As illustrated in Figure 4, DAG generates the most accurate attention heatmaps for intestinal metaplasia areas. All three comparative models exhibited a tendency to either concentrate on substantial non-intestinal metaplasia regions or neglect specific intestinal metaplasia foci. In contrast, DAG demonstrates a good concordance with pathological annotations, while maintaining robust capability in concentrating on both adjacent lesion clusters and distally scattered multifocal lesions. These findings suggest DAG achieves a strong balance between coarse-grained lesion localization and fine-grained boundary recognition.

### Ablation Study

**Effectiveness of key components of DAG.** We conduct comprehensive ablation studies to investigate the effectiveness of the key components in our proposed method, namely the offset prediction module (Offset), the edge weight module (Weight), and the spatial coordinate module (Coords). The results evaluated on four datasets are summarized in Table 2.

**(1) Offset Module.** The learnable offset module empowers the model to dynamically adjust the receptive field for neighboring patch selection, enabling enhanced capture of structural layouts and improved identification of lesion regions across WSIs. As evidenced by ablation studies on

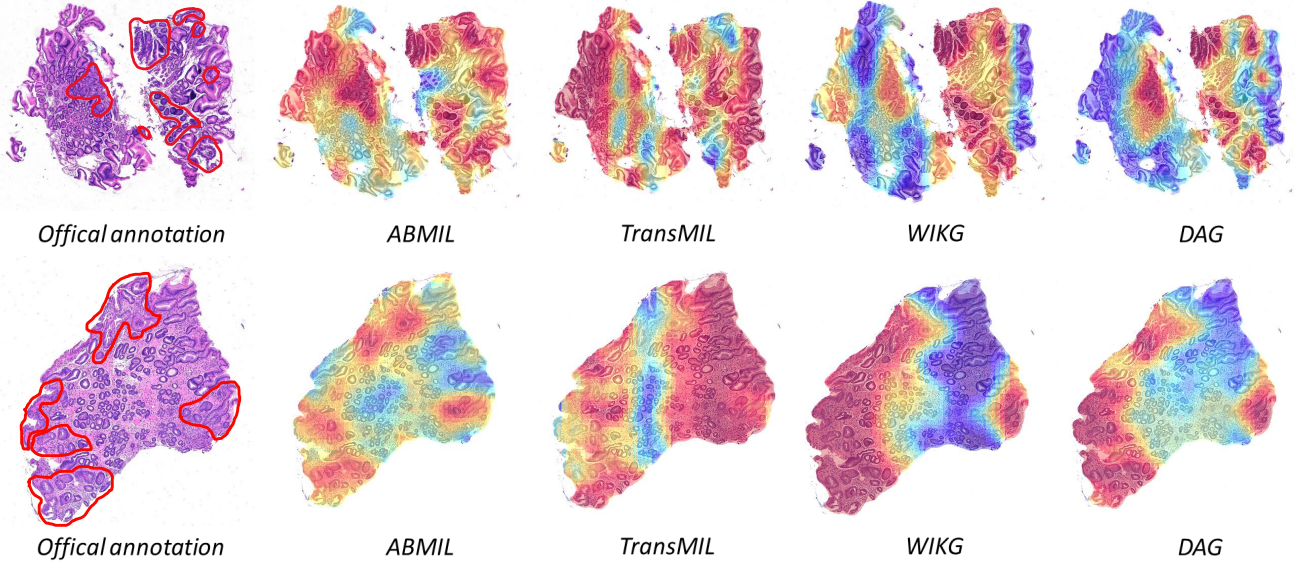


Figure 4: Visualization of DAG Attention Distribution Compared to Official Annotations on Gastric intestinal metaplasia dataset.

four datasets, incorporating the offset module consistently yields superior performance compared to its absence. These results demonstrate the module’s effectiveness in modeling fine-grained tissue structures and strengthening the model’s capacity to focus on critical pathological regions.

**(2) Edge Weight Module.** The edge weight module dynamically computes and updates attention weights between nodes and offset, indicating the relative importance of each neighbor during aggregation. In the ablation results across four datasets, removing the edge weights clearly leads to worse performance. This suggests that edge attention weights are essential for emphasizing highly correlated neighbors, which is necessary for accurate recognition of complex pathological structures.

**(3) Coordinate Module.** The coordinate module provides the model with absolute spatial positions of individual patches, facilitating the modeling of spatial dependencies and avoiding selecting distant unrelated patches as neighbors. Across all ablation studies, the integration of coordinate information consistently improves performance, highlighting its importance in holding tissue structural relationships and locating lesion areas.

Figure 5 presents the visualization of the ablation results. For the intestinal metaplasia (IM) grading task in gastritis, pathologists often focus on gland regions during diagnosis. The visualization from our proposed DAG demonstrates its ability to precisely distinguish each intestinal metaplasia gland and accurately delineate the gland boundaries. Moreover, thanks to the dynamically learnable offset mechanism, DAG is capable of performing long-range attention, effectively capturing distant intestinal metaplasia regions and localizing them with high accuracy. In addition, Figure 5 also illustrates the critical roles of the three key modules in DAG. Without the edge weight module, the model fails to assess

Dataset	Component			ACC	AUC	F1
	Offset	Weight	Coords			
COAD	✓	✓		84.73 <sub>3.08</sub>	94.39 <sub>0.55</sub>	82.47 <sub>2.73</sub>
	✓		✓	85.16 <sub>2.45</sub>	94.92 <sub>1.04</sub>	81.35 <sub>3.80</sub>
		✓	✓	85.38 <sub>2.36</sub>	94.82 <sub>0.24</sub>	82.74 <sub>2.38</sub>
	✓	✓	✓	<b>87.31<sub>1.59</sub></b>	<b>95.73<sub>0.56</sub></b>	<b>84.89<sub>1.50</sub></b>
IM	✓	✓		77.85 <sub>2.53</sub>	92.80 <sub>2.73</sub>	76.75 <sub>3.21</sub>
	✓		✓	78.76 <sub>4.52</sub>	93.88 <sub>1.92</sub>	77.60 <sub>4.29</sub>
		✓	✓	78.04 <sub>3.56</sub>	93.82 <sub>1.58</sub>	77.30 <sub>1.66</sub>
	✓	✓	✓	<b>80.39<sub>2.60</sub></b>	<b>95.24<sub>0.48</sub></b>	<b>79.27<sub>3.44</sub></b>
BRACS	✓	✓		57.35 <sub>1.50</sub>	89.21 <sub>0.69</sub>	56.94 <sub>1.46</sub>
	✓		✓	58.76 <sub>1.90</sub>	89.34 <sub>1.15</sub>	57.64 <sub>1.91</sub>
		✓	✓	56.15 <sub>1.46</sub>	88.67 <sub>1.54</sub>	54.43 <sub>2.90</sub>
	✓	✓	✓	<b>59.67<sub>1.34</sub></b>	<b>90.20<sub>0.81</sub></b>	<b>58.11<sub>1.17</sub></b>
Intestine	✓	✓		95.39 <sub>0.10</sub>	99.45 <sub>0.07</sub>	95.39 <sub>1.00</sub>
	✓		✓	93.92 <sub>1.23</sub>	99.09 <sub>0.14</sub>	93.86 <sub>1.32</sub>
		✓	✓	95.48 <sub>1.30</sub>	99.42 <sub>0.23</sub>	95.47 <sub>1.26</sub>
	✓	✓	✓	<b>96.36<sub>1.42</sub></b>	<b>99.46<sub>0.20</sub></b>	<b>96.33<sub>1.46</sub></b>

Table 2: Ablation study on the effectiveness of DAG components.

the importance of neighbor nodes during graph construction, resulting in incorrect attention allocation. Without spatial coordinates, the model loses awareness of distant lesion regions and fails to capture the underlying structural dependencies among patches. Besides, removing the offset module results in coarse-grained attention patterns. The model can roughly identify lesion regions but fail to recognize their precise morphological boundaries.

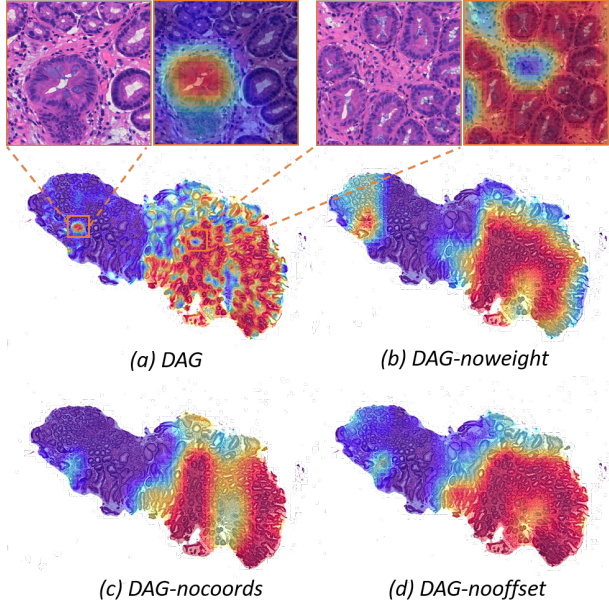


Figure 5: Attention distribution of different components: (a) Deformable attention graph with weight, coords and offset three modules. (b) Deformable attention graph without weight module. (c) Deformable attention graph without coords module. (d) Deformable attention graph without offset module.

**Effectiveness of Hyperparameter.** We conduct our ablation experiments on Hyperparameter  $topk$  and  $stride$ . The hyperparameter  $topk$  determines the number of neighboring nodes selected during the dynamic graph construction process. The hyperparameter  $stride$  controls the spatial sampling range during the dynamic graph construction.

**(1) Influence of Hyperparameter  $topk$ .** Figure 6 shows that a moderate number of neighbors achieves a good balance between computational efficiency and representational power. If  $topk$  is too small, the model captures limited information, potentially missing critical pathological structures. Conversely, setting  $topk$  too large may aggregate excessive irrelevant or noisy information, degrading the discriminative capability of the model.

**(2) Influence of Hyperparameter  $stride$ .** Table 3 presents the classification accuracy under different  $stride$  settings across four datasets. The results show that each dataset achieves optimal performance at different stride values. A smaller  $stride$  allows the model to focus on a more localized spatial region, thereby capturing fine-grained pathological structures more effectively. For example, in the in-

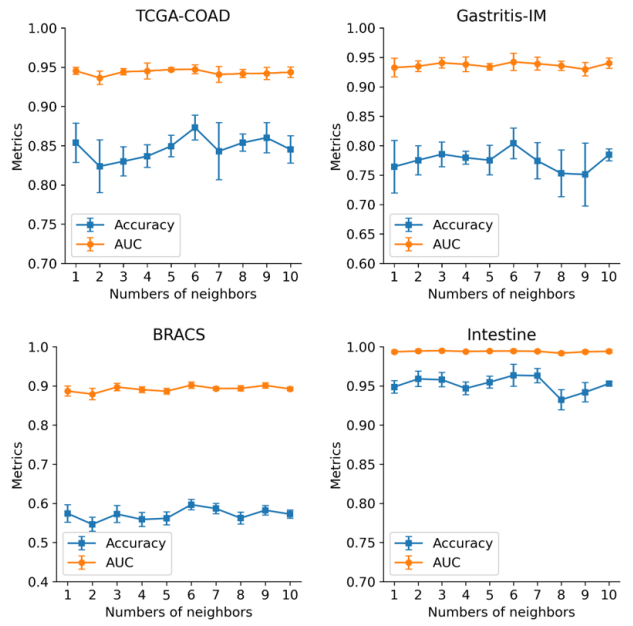


Figure 6: Classification results of AUC and ACC scores with different numbers of neighbor nodes on four datasets.

testinal metaplasia classification task, glandular structures are critical factors for diagnosing, and the model performs better with smaller strides. In contrast, a larger  $stride$  enables the model to perceive broader spatial dependencies and capture more global contextual information. For instance, the BRACS classification task emphasizes overall structural patterns of the tissue, thus achieving superior performance with larger strides.

Stride	BRACS	COAD	IM	Intestine
64	57.27 <sub>1.28</sub>	85.81 <sub>1.77</sub>	78.45 <sub>2.01</sub>	<b>95.30<sub>0.93</sub></b>
128	56.47 <sub>2.23</sub>	85.59 <sub>1.63</sub>	<b>80.39<sub>2.60</sub></b>	94.16 <sub>2.23</sub>
256	56.04 <sub>2.45</sub>	84.95 <sub>1.32</sub>	78.66 <sub>2.91</sub>	94.13 <sub>0.62</sub>
512	56.18 <sub>5.10</sub>	85.38 <sub>2.59</sub>	77.14 <sub>2.44</sub>	94.14 <sub>2.30</sub>
1024	<b>57.50<sub>1.06</sub></b>	<b>87.31<sub>1.59</sub></b>	79.78 <sub>2.73</sub>	94.89 <sub>1.12</sub>

Table 3: Accuracy of different stride values on four datasets.

## Conclusion and Future Work

In this paper, we propose DAG, a deformable attention-based graph neural network. By incorporating the actual spatial coordinates of patches, DAG constructs a dynamically weighted graph structure and introduces a deformable attention mechanism based on input features. Through the design of learnable offset modules, the model is able to dynamically capture structurally relevant regions from a global perspective, effectively modeling the complex tissue relationships inherent in pathological images. Extensive experiments and ablation studies conducted on four datasets demonstrate the effectiveness of DAG in recognizing pathological structures.

In addition, we observe that DAG achieves strong performance in entity-centered diagnostic tasks, demonstrating a clear ability to delineate well-defined structural boundaries. In future work, we plan to focus on clinically relevant tasks that emphasize entity-level recognition and further extend our approach to downstream applications such as pathological image segmentation.

## References

Afonso, M.; Bhawsar, P. M.; Saha, M.; Almeida, J. S.; and Oliveira, A. L. 2024. Multiple Instance Learning for WSI: A comparative analysis of attention-based approaches. *Journal of Pathology Informatics*, 15: 100403.

Ahmedt-Aristizabal, D.; Armin, M. A.; Denman, S.; Fookes, C.; and Petersson, L. 2022. A survey on graph-based deep learning for computational histopathology. *Computerized Medical Imaging and Graphics*, 95: 102027.

Chan, T. H.; Cendra, F. J.; Ma, L.; Yin, G.; and Yu, L. 2023. Histopathology whole slide image analysis with heterogeneous graph representation learning. In *Proceedings of the IEEE/CVF conference on computer vision and pattern recognition*, 15661–15670.

Chen, R. J.; Ding, T.; Lu, M. Y.; Williamson, D. F.; Jaume, G.; Song, A. H.; Chen, B.; Zhang, A.; Shao, D.; Shaban, M.; et al. 2024. Towards a general-purpose foundation model for computational pathology. *Nature medicine*, 30(3): 850–862.

Chen, R. J.; Lu, M. Y.; Shaban, M.; Chen, C.; Chen, T. Y.; Williamson, D. F.; and Mahmood, F. 2021. Whole slide images are 2d point clouds: Context-aware survival prediction using patch-based graph convolutional networks. In *International Conference on Medical Image Computing and Computer-Assisted Intervention*, 339–349. Springer.

Chen, Y.; Li, J.; Zhu, L.; Xu, Y.; Guan, T.; Shi, H.; He, Y.; and Han, A. 2025. Dynamic hypergraph representation for bone metastasis analysis. *Computer Methods and Programs in Biomedicine*, 108966.

Chikontwe, P.; Kim, M.; Jeong, J.; Sung, H. J.; Go, H.; Nam, S. J.; and Park, S. H. 2024. FR-MIL: Distribution re-calibration based multiple instance learning with transformer for whole slide image classification. *IEEE Transactions on Medical Imaging*.

Child, R.; Gray, S.; Radford, A.; and Sutskever, I. 2019. Generating long sequences with sparse transformers. *arXiv preprint arXiv:1904.10509*.

Gadermayr, M.; and Tschuchnig, M. 2024. Multiple instance learning for digital pathology: A review of the state-of-the-art, limitations & future potential. *Computerized Medical Imaging and Graphics*, 112: 102337.

Ilse, M.; Tomczak, J.; and Welling, M. 2018. Attention-based deep multiple instance learning. In *International conference on machine learning*, 2127–2136. PMLR.

Jaume, G.; Pati, P.; Bozorgtabar, B.; Foncubierta, A.; Anniciello, A. M.; Feroce, F.; Rau, T.; Thiran, J.-P.; Gabrani, M.; and Goksel, O. 2021. Quantifying explainers of graph neural networks in computational pathology. In *Proceedings of the IEEE/CVF conference on computer vision and pattern recognition*, 8106–8116.

Khazaaleh, S.; Alomari, M.; Rashid, M. U.; Castaneda, D.; and Castro, F. J. 2024. Gastric intestinal metaplasia and gastric cancer prevention: Watchful waiting. *Cleveland Clinic Journal of Medicine*, 91(1): 33–39.

Kumar, N.; Gupta, R.; and Gupta, S. 2020. Whole slide imaging (WSI) in pathology: current perspectives and future directions. *Journal of digital imaging*, 33(4): 1034–1040.

Li, B.; Li, Y.; and Eliceiri, K. W. 2021. Dual-stream multiple instance learning network for whole slide image classification with self-supervised contrastive learning. In *Proceedings of the IEEE/CVF conference on computer vision and pattern recognition*, 14318–14328.

Li, G.; Xu, D.; Cheng, X.; Si, L.; and Zheng, C. 2022. Simvit: Exploring a simple vision transformer with sliding windows. In *2022 IEEE International Conference on Multimedia and Expo (ICME)*, 1–6. IEEE.

Li, H.; Yang, F.; Zhao, Y.; Xing, X.; Zhang, J.; Gao, M.; Huang, J.; Wang, L.; and Yao, J. 2021. DT-MIL: deformable transformer for multi-instance learning on histopathological image. In *International Conference on Medical Image Computing and Computer-Assisted Intervention*, 206–216. Springer.

Li, J.; Chen, Y.; Chu, H.; Sun, Q.; Guan, T.; Han, A.; and He, Y. 2024. Dynamic graph representation with knowledge-aware attention for histopathology whole slide image analysis. In *Proceedings of the IEEE/CVF conference on computer vision and pattern recognition*, 11323–11332.

Liang, M.; Chen, Q.; Li, B.; Wang, L.; Wang, Y.; Zhang, Y.; Wang, R.; Jiang, X.; and Zhang, C. 2023. Interpretable classification of pathology whole-slide images using attention based context-aware graph convolutional neural network. *Computer methods and programs in biomedicine*, 229: 107268.

Ling, X.; Ouyang, M.; Wang, Y.; Chen, X.; Yan, R.; Chu, H.; Cheng, J.; Guan, T.; Tian, S.; Liu, X.; et al. 2024. Agent aggregator with mask denoise mechanism for histopathology whole slide image analysis. In *Proceedings of the 32nd ACM International Conference on Multimedia*, 2795–2803.

Liu, Z.; Lin, Y.; Cao, Y.; Hu, H.; Wei, Y.; Zhang, Z.; Lin, S.; and Guo, B. 2021. Swin transformer: Hierarchical vision transformer using shifted windows. In *Proceedings of the IEEE/CVF international conference on computer vision*, 10012–10022.

Lu, M. Y.; Williamson, D. F.; Chen, T. Y.; Chen, R. J.; Barbieri, M.; and Mahmood, F. 2021. Data-efficient and weakly supervised computational pathology on whole-slide images. *Nature biomedical engineering*, 5(6): 555–570.

Maron, O.; and Lozano-Pérez, T. 1997. A framework for multiple-instance learning. *Advances in neural information processing systems*, 10.

Pati, P.; Jaume, G.; Fernandes, L. A.; Foncubierta-Rodríguez, A.; Feroce, F.; Anniciello, A. M.; Scognamiglio, G.; Brancati, N.; Riccio, D.; Di Bonito, M.; et al. 2020. Hact-net: A hierarchical cell-to-tissue graph neural network for histopathological image classification. In *International Workshop on Uncertainty for Safe Utilization of Machine Learning in Medical Imaging*, 208–219. Springer.

Russell, T. D.; Jindal, S.; Agunbiade, S.; Gao, D.; Troxell, M.; Borges, V. F.; and Schedin, P. 2015. Myoepithelial cell differentiation markers in ductal carcinoma in situ progression. *The American journal of pathology*, 185(11): 3076–3089.

Shao, Z.; Bian, H.; Chen, Y.; Wang, Y.; Zhang, J.; Ji, X.; et al. 2021. Transmil: Transformer based correlated multiple instance learning for whole slide image classification. *Advances in neural information processing systems*, 34: 2136–2147.

Su, Y.; Bai, Y.; Zhang, B.; Zhang, Z.; and Wang, W. 2021. HAT-Net: A Hierarchical Transformer Graph Neural Network for Grading of Colorectal Cancer Histology Images. In *BMVC*, 412.

Vaswani, A.; Shazeer, N.; Parmar, N.; Uszkoreit, J.; Jones, L.; Gomez, A. N.; Kaiser, Ł.; and Polosukhin, I. 2017. Attention is all you need. *Advances in neural information processing systems*, 30.

Wang, J.; Mao, Y.; Guan, N.; and Xue, C. J. 2024a. Advances in multiple instance learning for whole slide image analysis: Techniques, challenges, and future directions. *arXiv preprint arXiv:2408.09476*.

Wang, K.; Zheng, F.; Cheng, L.; Dai, H.-N.; Dou, Q.; and Qin, J. 2024b. Breast cancer classification from digital pathology images via connectivity-aware graph transformer. *IEEE Transactions on Medical Imaging*, 43(8): 2854–2865.

Wang, W.; Xie, E.; Li, X.; Fan, D.-P.; Song, K.; Liang, D.; Lu, T.; Luo, P.; and Shao, L. 2021. Pyramid vision transformer: A versatile backbone for dense prediction without convolutions. In *Proceedings of the IEEE/CVF international conference on computer vision*, 568–578.

Wang, Z.; Ma, J.; Gao, Q.; Bain, C.; Imoto, S.; Lio, P.; Cai, H.; Chen, H.; and Song, J. 2024c. Dual-stream multi-dependency graph neural network enables precise cancer survival analysis. *Medical Image Analysis*, 97: 103252.

Xia, Z.; Pan, X.; Song, S.; Li, L. E.; and Huang, G. 2022. Vision transformer with deformable attention. In *Proceedings of the IEEE/CVF conference on computer vision and pattern recognition*, 4794–4803.

Xia, Z.; Pan, X.; Song, S.; Li, L. E.; and Huang, G. 2023. Dat++: Spatially dynamic vision transformer with deformable attention. *arXiv preprint arXiv:2309.01430*.

Yao, J.; Zhu, X.; Jonnagaddala, J.; Hawkins, N.; and Huang, J. 2020. Whole slide images based cancer survival prediction using attention guided deep multiple instance learning networks. *Medical image analysis*, 65: 101789.

Zaheer, M.; Guruganesh, G.; Dubey, K. A.; Ainslie, J.; Alberti, C.; Ontanon, S.; Pham, P.; Ravula, A.; Wang, Q.; Yang, L.; et al. 2020. Big bird: Transformers for longer sequences. *Advances in neural information processing systems*, 33: 17283–17297.

Zhu, X.; Hu, H.; Lin, S.; and Dai, J. 2019. Deformable convnets v2: More deformable, better results. In *Proceedings of the IEEE/CVF conference on computer vision and pattern recognition*, 9308–9316.

Zhu, X.; Su, W.; Lu, L.; Li, B.; Wang, X.; and Dai, J. 2020. Deformable detr: Deformable transformers for end-to-end object detection. *arXiv preprint arXiv:2010.04159*.